A novel J-shape antenna array for simultaneous MR-PET or MR-SPECT imaging

Chang-Hoon Choi, Suk-Min Hong, Jörg Felder, *Member, IEEE,* Lutz Tellmann, Jürgen Scheins, Elena Rota Kops, Christoph Lerche, N. Jon Shah

***Abstract*—Simultaneous MR-PET/-SPECT is an emerging technology that capitalises on the invaluable advantages of both modalities, allowing access to numerous sensitive tracers and superior soft-tissue contrast alongside versatile functional imaging capabilities. However, to optimise these capabilities, concurrent acquisitions require the MRI antenna located inside the PET/SPECT field-of-view to be operated without compromising any aspects of system performance or image quality compared to the stand-alone instrumentation. Here, we report a novel gamma-radiation-transparent antenna concept. The end-fed J-shape antenna is particularly adept for hybrid ultra-high field MR-PET/-SPECT applications as it enables all highly attenuating materials to be placed outside the imaging field-of-view. Furthermore, this unique configuration also provides advantages in stand-alone MR applications by reducing the amount of coupling between the cables and the antenna elements, and by lowering the potential specific absorption rate burden. The use of this new design was experimentally verified according to the important features for both ultra-high field MRI and the 511 keV transmission scan. The reconstructed attenuation maps evidently showed much lower attenuation (~15%) for the proposed array when compared to the conventional dipole antenna array since there were no high-density components. In MR, it was observed that the signal-to-noise ratio from the whole volume obtained using the proposed array was comparable to that acquired by the conventional array which was also in agreement with the simulation results. The unique feature, J-shape array, would enable simultaneous MR-PET/-SPECT experiments to be conducted without unduly compromising any aspects of system performance and image quality compared to the stand-alone instrumentation.**

***Index Terms*—J-pole, PET-MR, PET/MRI, SPECT, Gamma radiation transparent.**

I. INTRODUCTION

Magnetic resonance imaging (MRI), positron emission tomography (PET) and single-photon emission computed tomography (SPECT) are well-established medical imaging modalities used in current routine clinical practice [1]. PET/SPECT imaging uses a variety of radioactive tracers that target different metabolic and molecular pathways, giving valuable insights into physiological and metabolic processes with both a high level of specificity and sensitivity [2-5]. The specific biodistribution of the injected radioactive tracer reveals important information relating to the function and dysfunction of the particular organ, tissue or region. The underlying principle of PET image formation is that positrons are emitted from the radioactive tracer and annihilate into two back-to-back gamma photons. The PET scanner, comprising a large number of scintillation detectors, is arranged as a full detector ring to cover the subject volume and detects these photons to generate PET images. In the case of SPECT, only one gamma photon is emitted, which moves away from the site of decay in a straight line. The SPECT scanner, therefore, requires a collimator which is normally arranged as one or more rotating panel detector(s) covering the subject volume to detect these photons and generate SPECT images. Due to the limitations of using computed tomography in combination with PET or SPECT [6, 7], e.g., soft tissue contrast, radiation exposure and no simultaneous measurements, the development and clinical use of hybrid scanners with MRI has gradually increased in recent years [8-15]. In contrast to PET/SPECT, MRI typically using hydrogen nuclei (^{1}H), bestows high-quality structural/anatomical imaging capability, with both outstanding soft tissue contrasts and functional information. The MR sensitivity increases proportionally to the magnetic field strength, offering a number of benefits in MRI, such as high resolution and improved signal-to-noise ratio (SNR). Thus, there is a trend towards stronger field strengths and 7 T systems are now widely available for research and clinical examinations. Moreover, 10.5 T and 11.7 T whole-body MRI systems have been installed and the development of a 14 T human MRI system is under consideration [16-18].

Integrated simultaneous PET/SPECT and MRI is strenuous but capitalises on the advantages afforded by both modalities, allowing a unique combination of morphology and functional molecular imaging. In a concurrent MR-PET or -SPECT acquisition, a radiofrequency (RF) coil or antenna for MRI experiments is required. This would most likely be placed inside the PET or SPECT active imaging region. Standard MRI RF coils or antennas are not PET and SEPCT optimised and are focused only on MRI requirements. Thus, they contain strongly attenuating and scattering materials, e.g., capacitors or coaxial cables, at nonuniformly distributed points in the PET or SPECT field-of-view (FOV). The resultant count loss or reduction in

This work was supported in part by the Helmholtz Validation Fund, "Next generation BrainPET scanner for 7 T MRI" Grant Nr. HVF-0051.

C.-H. Choi (c.choi@fz-juelich.de), S.-M. Hong (s.hong@fz-juelich.de), L. Tellmann (l.tellmann@fz-juelich.de), J. Scheins (j.scheins@fz-juelich.de), E. Rota Kops (e.rota.kops@fz-juelich.de), C. Lerche (c.lerche@fz-juelich.de) are with the Institute of Neuroscience and Medicine – 4 (INM-4), Forschungszentrum Jülich, Jülich, Germany. J. Felder (j.felder@fz-juelich.de) is with INM-4, Forschungszentrum Jülich, Jülich, Germany, with RWTH University, Aachen, Germany. N. J. Shah (n.j.shah@fz-juelich.de) is with INM-4 and INM-11, Forschungszentrum Jülich, Jülich, Germany, with JARA - BRAIN - Translational Medicine, Aachen, Germany and with the Department of Neurology, RWTH Aachen University, Aachen, Germany. Corresponding author: C.-H. Choi.

the number of true coincidences reduces the sensitivity of the system [19-22]. It may also cause significant quantification errors in the PET and SPECT images [23-25] and severe artefacts, such as streak-like artefacts [22, 26-29]. While it may be necessary to correct for the attenuation of the RF probe located inside the FOV of PET and SPECT, such corrections can be laborious, and artefacts may not always be fully removed [25, 29, 30]. Furthermore, even when the attenuation of the coil is corrected, the detection sensitivity of PET and SPECT is reduced, leading to a degradation in the quality of PET or SPECT images. It is, therefore, crucial to minimise any potential attenuation of photons in order to achieve the optimal PET and SPECT images while at the same time maintaining the maximum MR image quality. An additional consideration in terms of the MRI coil is its capability of providing anatomical images of the object covering the entire PET or SPECT FOV, which enables a useful attenuation map to be generated for accomplishing accurate PET or SPECT image reconstruction. Due to the greater number of element parts, the design and development of a multi-channel antenna array for use in a combined system poses new challenges [21, 31, 32] and requires a different approach to the conventional RF antenna arrays at ultra-high field (≥ 7 tesla) - where an RF wavelength in tissue is shorter than the imaging object. The use of a radiating antenna, such as a dipole antenna [33], travelling-wave antenna [34] or the use of a magnetic metamaterial [35, 36] is unavoidable since they provide extended penetration with a symmetrical RF field.

Therefore, when constructing RF antenna arrays it is especially important to adopt a targeted design approach that takes PET and SPECT compatibility and requirements (i.e., minimum attenuation and scattering effect) into account, while also maximising the MR detection capability [21-23, 32, 37, 38]. In this context, we introduce a novel design concept, namely, a J-pole or J-shape antenna array. This completely new approach to building a multi-channel RF antenna array overcomes the aforementioned constraints and fulfils the optimal conditions for the simultaneous operation. In addition, the rationale for this novel design is to provide a highly effective, high performance, yet inexpensive and simple to construct antenna array for simultaneously operating hybrid systems as well as for standalone ultra-high field MRI systems.

II. MATERIALS AND METHODS

A. J-shape antenna array

An overview of the single-channel J-shape antenna design is shown in Fig. 1a. Compared to a traditional loop coil, a radiating antenna, such as a dipole or a monopole antenna, can transmit higher levels of RF deeper in the subject's body, which is particularly beneficial in human head MR imaging at ultra-high field strengths (≥ 7 T) [39]. As a type of radiating antenna, the J-shape antenna is a novel and extremely attractive concept which, to the best of our knowledge, has never been employed in medical imaging, although it is often used for other purposes relating to the antenna engineering [40]. This antenna comprises an MR compatible, gamma-radiation-transparent and minimal gamma photon scattering radiating segment (physical length of ~ λ/2 in a free space), and an electrically connected feeding part (~ λ/4). The material of this radiating segment is a thin conducting pattern made of, e.g., copper or aluminium, which can be gamma-radiation-transparent, thus providing negligible attenuation and scattering influence (i.e., no PET or SPECT performance degradation). The feeding part mainly consists of a matching unit, which can be applied to achieve the impedance matching of the antenna with the impedance of an RF system output. The fine impedance matching can be achieved by sliding the connection of the feed line up and down along the feeding part or by adjusting the capacitor inserted in the matching network. Moreover, and most importantly, unlike the conventional dipole antenna [33], this J-shape antenna is end-fed, making it particularly suitable for hybrid MR-PET or -SPECT applications since all high-density materials, such as capacitors, coaxial cables, can be placed at one side of the assembly: obviously far outside the imaging FOV. This unique feature also provides advantages in MR only applications by reducing a significant amount of RF coupling or interference between the coaxial cables and the antenna elements and by lowering the potential specific absorption rate (SAR) burden in the imaging region.

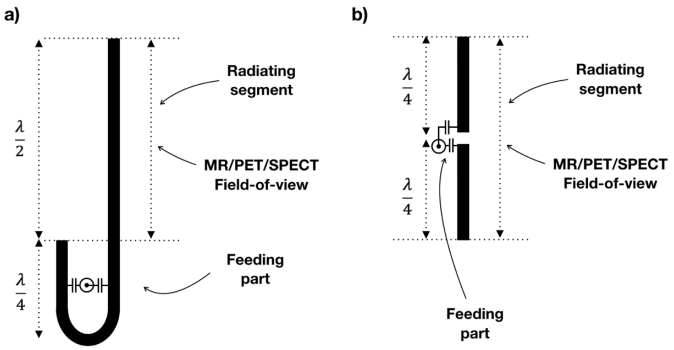

Fig. 1. Design of a single radiating antenna element. Schematic diagrams of proposed J-shape antenna a) and dipole antenna used mostly in ultra-high field MRI b).

Fig. 2 displays the multi-channel antenna arrays: The J-shape antenna (top) and the conventional dipole antenna (bottom), in which the individual antenna element is evenly distributed around the volume of interest within the PET or SPECT imaging FOV. In order to enable fair comparison with the conventional dipole array, the J-shape antenna array was limited to six channels. However, the number of channels can be readily extended to higher numbers, e.g., eight. Moreover, the length of these arrays was selected so that the chin area would be covered, allowing the potential attenuation correction based on a co-registered MR image to be performed sufficiently, which was a problem using the existing commercial RF coil array due to the missing array elements in the region. If required, tuning to the desired resonance frequency can be achieved by shortening or adjusting the antenna length or by modifying the antenna pattern to a snake shape [41]. It is also possible to tailor the antenna array to the

object being scanned by inserting meander ends or inductors (placed in the feeding unit area) [33]. Avoiding the use of highly attenuating inductors would also be advantageous for the conventional dipole array.

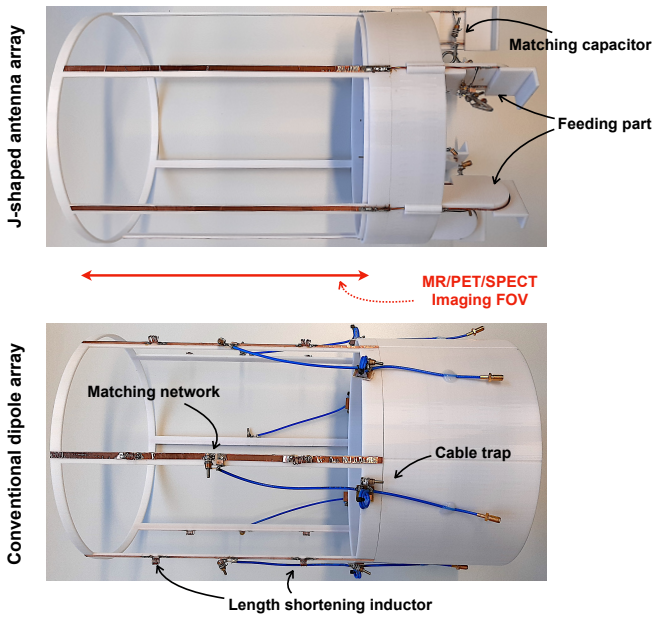

Fig. 2. Pictures of the proposed multi-channel J-shape antenna array (top) and the ordinary, multi-channel dipole antenna array (bottom). It is clear that the proposed J-shape antenna array does not include any components within the imaging FOV.

B. Design and construction of the J-shape antenna array and reference dipole antenna array

The proposed RF antenna array, adapted for hybrid MR-PET or MR-SPECT systems, includes J-shape antennas equally distributed around a target imaging volume. Each J-shape antenna element comprises a gamma-radiation-transparent radiating segment and a feeding unit, wherein both parts are connected electrically. The gamma-radiation-transparent segment does not include any components and only presents antenna traces made of thin copper (35 µm thickness and 6 mm width) on a 3 mm plastic antenna former. Thus, this does not generate any deleterious effects on the acquisition of the PET or SPECT data and provides the benefit of negligible attenuation and scattering artefacts. The feeding unit is located outside of the MR or PET imaging region and contains a matching network and a coaxial cable connecting to an RF interface. These components are positioned at one side of the antenna to avoid any interference with the antenna itself. The feeding part of the antenna can be bent vertically towards the inside of the coil former or along the outside surface of the coil former, as shown in the supplementary material (Fig. S1). In order to compare and evaluate the performance of the J-shape antenna array, we have also built a reference array in the standard dipole antenna array format.

Both antenna arrays were tuned to 297 MHz (corresponding to the Larmor frequency of a 7 T MRI system). The tuning of each antenna array was initially achieved using the physical length of the antenna pattern and the matching was managed by the use of non-magnetic fixed (C series, Dalicap, China) and variable (Voltronics, USA) capacitors. In the case of the J-shape antenna, the location of the feeding points influences the matching condition which could also be finely adjusted using the variable capacitor. In order to shorten the length of the reference array, inductors were inserted which can be replaced by the introduction of meanders onto the antenna pattern. No decoupling methods were implemented since our focus was on validating the fundamental behaviour and field distribution of the J-shape antenna array on the uniform phantom.

C. Design and construction of the RF chain and interface

A photograph and a schematic diagram of the RF interface commonly used to test both the proposed and the reference antenna arrays are shown in the supplementary material (Fig. S2a and S2b, respectively). The interface, including a 6-way (3-way + 2-way) Wilkinson power divider and active transmit/receive (T/R) switches, was designed and constructed. The Wilkinson units were utilised in order to divide the transmit power into six channels, and phase differences among channels were controlled by adjusting the coaxial cable length. This transmit divider was then connected to the input of transmission of each T/R switch, and preamplifiers were protected by means of π-networks and PIN-diodes controlled by the MRI scanner. Cable traps were used on both the input and output of the RF chain in order to minimise common-mode interference. The response (Tx insertion loss and Tx phase) of the entire RF chain and interface (from the system-end plug to the coil-end plug) was characterised on the laboratory bench using a vector network analyser.

D. Electromagnetic simulation

In order to anticipate the characteristics of the J-shape antenna array, frequently utilised finite integration technique simulations were carried out at 7 T using the CST Studio Suite (CST AG, Darmstadt, Germany), and the results were compared to the conventional dipole antenna array. The antenna arrays were loaded either with a 14 cm diameter spherical phantom with the dielectric properties of conductivity $\sigma = 0.5$ S/m and permittivity $\varepsilon = 80$ presenting a similar load with the average human head [42] or with the head and a part of shoulders of the Duke voxel model (IT'IS-Foundation, Zurich, Switzerland). The voxel size of Duke was 2 mm × 2 mm × 2 mm. The six J-shape antenna elements were equally distributed around the volume and driven in a circularly polarised mode. All capacitors and inductors were represented by 50 Ω ports in a field simulation, allowing modification of the values of the capacitors, inductors and external ports in a circuit co-simulation [43]. The feeding port of each antenna element was driven by six external voltage sources containing an identical amplitude of 1 volt and an equally distributed phase (0/60/120/180/240/300°). Both the J-shape antenna array and the conventional dipole antenna array were tuned to 297 MHz and matched to 50 Ω in the co-simulation. After all components were successfully determined, a final co-simulation was

conducted to obtain the field distribution in the simulation domain. The PET shield was also included into the simulation model since this could influence the performance of the antenna arrays. The dimension of the PET shield (diameter = 360 mm and length = 634 mm) was selected to be the same as the brain PET insert system currently under construction [44]. The results of the transmit efficiency and SAR_{global} and $SAR_{10g,Max}$ generated by the arrays were analysed and compared. For the phantom results, the average B_1^+ field strengths were calculated across the whole volume of the phantom, while for the head model, the B_1^+ values were only calculated within the brain region. The transmit efficiency was scaled to accomplish the accepted power of 1 W for the phantom. With respect to the Duke model, the absorbed power of 1W and $SAR_{10g,Max}$ of 1W were additionally considered with and without the PET shield [45-47]. The SAR values were normalised to achieve the average transmit efficiency of 1 μT in the brain area.

E. MR bench measurements

A 2-litre spherical water phantom was prepared, doped with 3.75 g $NiSO_4$ × 6 H_2O × 5 g NaCl per 1000 g H_2O. A polydimethylsiloxane oil phantom provided by the manufacturer (Siemens Healthineers, Erlangen, Germany) was also used for the evaluation of both antenna arrays. The performance of both antenna arrays was initially evaluated on the bench using the network analyser (ZNB4, Rohde & Schwarz, Germany).

F. 511 keV transmission measurements

In order to verify the effect in the transmission performance as a result of the insertion of the proposed J-shape antenna array, transmission scans at 511 keV were carried out on a dedicated PET Scanner (ECAT Exact HR+, Siemens Healthineers, Erlangen, Germany) in which three rotating Ge^{68}/Ga^{68} rod sources (approximately, 150 MBq each) are equipped. Transmission measurements for both the proposed array and for the conventional array were performed separately over two hours in order to obtain high count rate statistics. For comparison, reference blank scans were also acquired with an identical scan time. In order to represent the attenuation coefficients of the different antenna array designs used in this study as images, the ratios of the transmission scan and the blank scan were reconstructed with the ordered subset expectation maximisation (6 iterations, 16 subsets) algorithm into 153 planes with 256 × 256 voxels per plane (plane thickness of 2.425 mm, pixel size of 2.57 mm × 2.57 mm). Corrections for random and scattered coincidences and for decay between transmission and blank scans were applied during the reconstruction. In addition, the acquired coincidences of the transmission and the blank scans were organised into sinograms (63 planes, 144 angle steps, 288 radial distance steps). The decay of the Ge^{68}/Ga^{68} transmission sources was corrected and the ratio of the transmission and the blank sinograms was computed. For estimating the total attenuation of the different antenna arrays, the ratio of total counts of the transmission and the blank scans was also calculated.

G. MR imaging experiments

All MR experiments were carried out on a 7 T Terra scanner (Siemens Healthineers, Erlangen, Germany) using a 2D FLASH sequence. The parameters were: repetition time = 3 s, echo time = 2.64 ms, number of averages = 1, slice thickness = 3 mm, flip angle = 90°, acquisition time = 3:33 minutes, matrix size = 192 × 256 and FOV = 187 mm × 250 mm. The power required for a 90-degree reference pulse was determined by sweeping a range of RF powers and computing the SNRs in a predetermined ROI. In order to calculate SNRs, the equation, $\left(\frac{\text{Signal mean}}{\text{Noise standard deviation}}\right)$ was used, in which the signal mean value in the selected ROI covering both the entire (red dashed circle) and the central area of the sphere phantom (e.g., yellow dotted circle in Fig. 7) is divided by the standard deviation of the noise image (i.e. the identical ROI but acquired with Tx power = 0). Both sagittal images obtained using the reference dipole antenna array and the proposed J-shape antenna array were compared. Oil phantom images in the axial plane showing homogenous B_1 are also included in Fig. 7.

III. RESULTS

A. Gamma-radiation-attenuation evaluation of the J-shape antenna array

Fig. 3 shows the attenuation maps in various positions of the antenna arrays, characterising each antenna array as well as a 3 mm plastic former. These cross-sectional slices were defined according to the position of the components in a conventional dipole array since, importantly, the proposed J-shape antenna array has no such components (only thin copper pattern; negligible effect on the attenuation) in the PET/SPECT sensitive FOV: Position 1 (P1) - the region where the co-axial cables (MULTIFLEX_86, Huber & Suhner, Germany) is present on the top of the 35 μm thin copper antenna pattern; P2 - the region where the length shortening inductors as well as the coaxial cables are located; P3 - the region where the matching network (incl. non-magnetic fixed and variable capacitors) is shown; P4 - the region where the inductors are included; P5 - the region where only thin copper pattern exists. The maps evidently show no degradation in attenuation for the proposed array, whereas relatively high attenuation was detected in the conventional dipole antenna array at several locations, in which the capacitors, inductors and co-axial cables are placed. The soldering tin used to attach the components to the antenna elements in the PET or SPECT detector active region also influences the attenuation, which could be a problem [22]. Unfortunately, in the conventional antenna array, these items are not removable from the active imaging region of PET and SPECT.

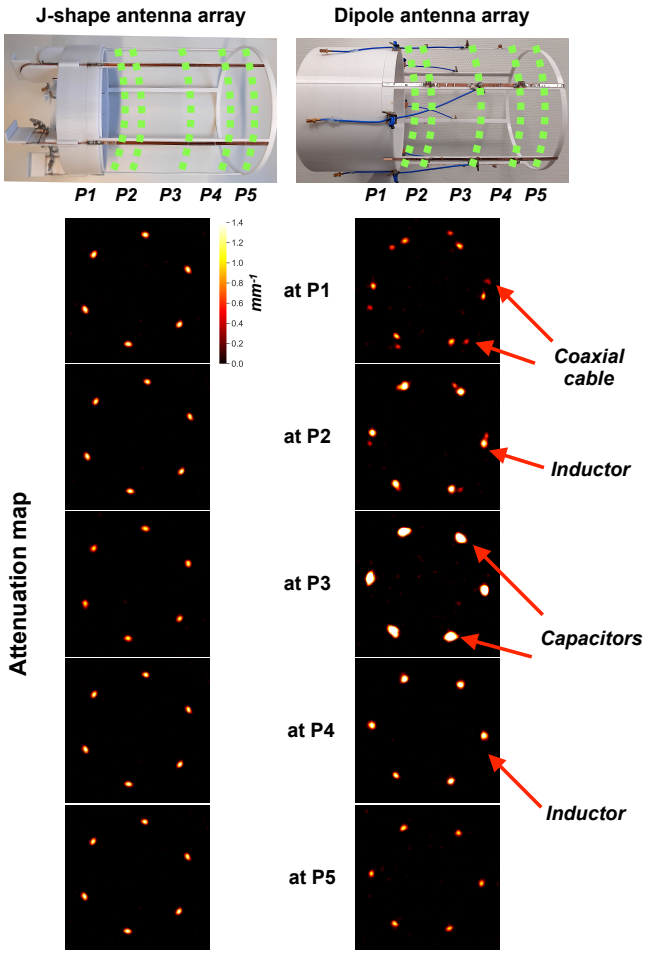

Fig. 3. Attenuation maps of the proposed J-shape antenna array (top) and of the reference dipole antenna array (bottom) in five cross-sectional areas (Position 1 (P1) ~ Position 5 (P5)). An enlarged, single-channel dipole antenna picture with attached components is included in the supplementary material (Fig. S3).

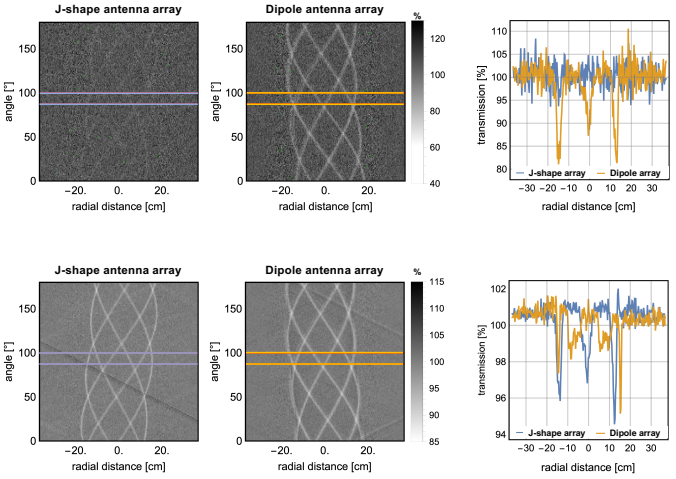

Fig. 4. Attenuation sinogram of the 511 keV transmission scans and blank scans within the region located at P3 in Fig. 3. The images in the top row show single sinogram planes for the J-shape antenna array (left), dipole antenna array (middle) in the axial plane, and their associated line profiles (averaged over 10 angles) within the region highlighted with the blue or orange lines (right). Sinograms and line profiles averaged over all 63 transversal sinogram planes are shown in the bottom row.

In Fig. 4, the ratio of transmission to blank sinogram of the 511 keV transmission scans within the region located at P3 in Fig. 3 is shown. The attenuation of the antenna components, including the copper pattern as well as the plastic former, was determined by computing the single plane and the attenuation averaged over all 63 transversal planes. As a result, it was observed that the attenuation for the conventional antenna array was significantly higher (~ 18%) in the planes with the inserted components compared to the attenuation observed with the proposed array (~ 5%), while similar averaged attenuation values (approximately 5%) were obtained for those gamma photons that mainly traverse the antenna structural parts. Owing to the large surface without any material and no attenuation of the gamma photons, the total attenuation of both arrays was less than 0.2%.

B. MR performance evaluation of the J-shape antenna array at 7 T

The various design concepts of the J-shape antenna array were first verified using a finite integration technique simulation. In Fig. 5, the illustrations in the top row show the simulation models of the proposed antenna array with a sphere phantom inside (left column) and the Duke human head model [48] with (right column)/without the shield (middle column). The second row of the figure shows simulated B_1^+ distributions of the phantom in the sagittal (top) and the axial (bottom) imaging planes of the proposed J-shape antenna array (left columns) and of the conventional dipole antenna array (right columns) at 7 T. The transmit efficiency map shown here for the phantom, was scaled to achieve the accepted power of 1 W, whereas the maps for the Duke model with/without the shield were scaled to accomplish the $SAR_{10g,Max}$ of 1W. The white straight and contour lines drawn in the Duke model specify the selected axial slice and the brain region, respectively. These were used to calculate the average B_1^+ and SAR values, shown in the table in the bottom row.

As indicated, the performance, particularly B_1^+ transmission efficiency, of the J-shape antenna array is comparable to the conventional antenna array, whereas relating to local and global SAR ($SAR_{10g,\,Max}$ and SAR_{global}, respectively), the proposed J-shape antenna array has also shown to be similar to the reference array. The proposed array provided an average B_1^+ efficiency of 0.31 $\mu T/\sqrt{W_{accepted}}$ over the whole volume of the phantom. The figure also depicts the average B_1^+ efficiency of 0.52 $\mu T/\sqrt{W_{SAR10g,Max}}$, SAR_{global} of 0.83 W/kg and $SAR_{10g,\,Max}$ of 3.77 W/kg over the Duke human brain model without the shield. Nearly similar B_1^+ (0.32 $\mu T/\sqrt{W_{accepted}}$ on the phantom / 0.52 $\mu T/\sqrt{W_{SAR10g,Max}}$) and $SAR_{10g,\,Max}$ (3.74 W/kg) but higher SAR_{global} result (1.01 W/kg) on the Duke model without the shield were acquired with the reference array. The figure further shows that the radiation loss was quite considerable for both types of array and resulted in efficiency loss. With the shield, the radiation loss appeared to be significantly reduced, which helped to improve the B_1^+ efficiencies, particularly, when normalised using the accepted and absorbed power [47, 49, 50].

Although a small number of studies have reported the possibility of reducing SAR by using a passive driven antenna [51] or by increasing the distance between the subject and the

antenna [52], as this J-shape antenna array is not affected by this problem, no additional measures are required. Since the feeding of the J-shape antenna array is located close to the top part of the head, the B_1^+ field in the region tends to be higher and may need to be optimised further in the future.

As shown in Fig. 6, the characteristics of the RF interface (a) and scattering parameters (S-parameter) for the J-shape (b) and dipole (c) antenna arrays were recorded. The 6-way splitter was found to be operating correctly, as the power divider and the output phase of each channel are seen to be well adjusted (maximum offset of -1.89° from the expected value). The S-parameter matrices show tuning, impedance matching and coupling conditions between array elements loaded with the spherical water phantom. The noise correlation matrices of both arrays were also obtained as shown in Fig. 6d (J-shape antenna array) and 6e (dipole antenna array).

Fig. 7 (top row) displays the multi-slice MR images measured on the spherical water phantom using the J-shape antenna array and the reference dipole antenna array at 7 T. The calculated relative SNRs (signal mean / noise standard deviation) in the red ROI (whole area) and in the yellow ROI (centre region) are 801 (568 / 0.709) and 1616 (1120 / 0.693) for the proposed array and are 802 (680 / 0.848) and 1322 (1026 / 0.776) for the conventional array. The SNR result in the whole volume obtained using both arrays is almost identical, which also conforms to the simulation results. Since the acquisition was carried out using a circularly-polarised mode, the central brightening [53], a known effect at ultra-high field, is seen in the water phantom. However, images (bottom row) with a uniform B_1 were observed with the oil phantom.

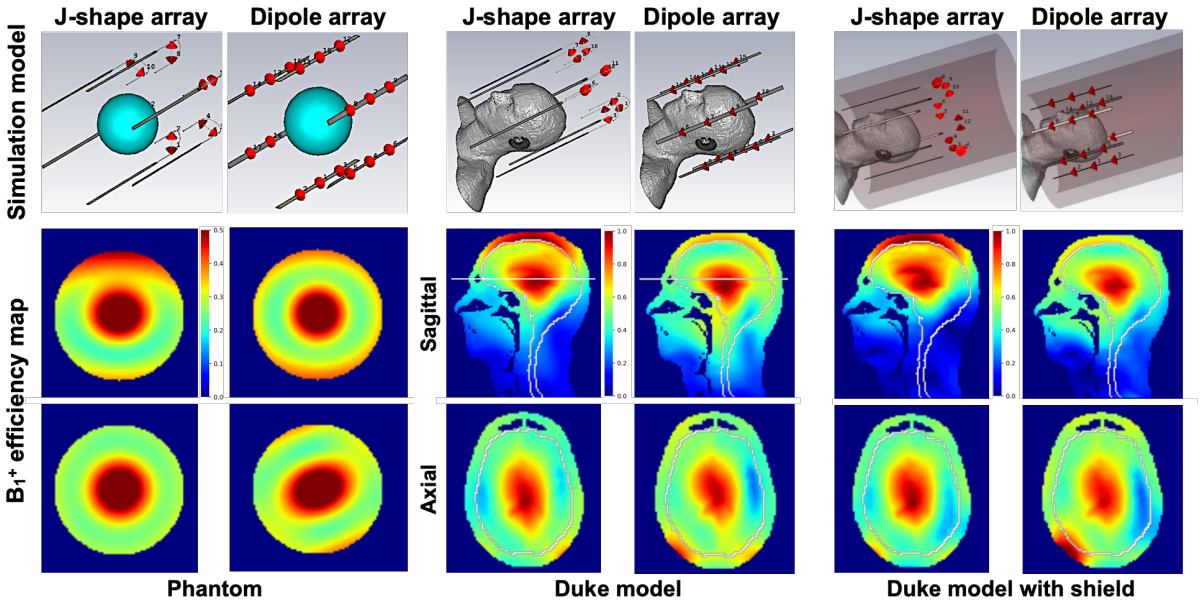

Simulation Model	Properity	J-shape antenna array	Dipole antenna array
Phantom	B_1^+ efficiency ($\mu T/\sqrt{W_{accepted}}$)	0.31	0.32
Duke without shield	B_1^+ efficiency ($\mu T/\sqrt{W_{accepted}}$)	0.26	0.28
	B_1^+ efficiency ($\mu T/\sqrt{W_{absorbed}}$)	0.45	0.41
	B_1^+ efficiency ($\mu T/\sqrt{W_{SAR\_10g,Max.}}$)	0.52	0.52
	Radiation loss	0.65	0.52
	Global SAR (W/kg)	0.83	1.01
	Max. 10 g SAR (W/kg)	3.77	3.74
Duke with shield	B_1^+ efficiency ($\mu T/\sqrt{W_{accepted}}$)	0.36	0.33
	B_1^+ efficiency ($\mu T/\sqrt{W_{absorbed}}$)	0.40	0.37
	B_1^+ efficiency ($\mu T/\sqrt{W_{SAR\_10g,Max}}$)	0.50	0.51
	Radiation loss	0.17	0.20
	Global SAR (W/kg)	0.93	1.04
	Max. 10 g SAR (W/kg)	4.01	3.92

Fig. 5. Simulated B_1^+ distribution maps and SAR values for a phantom and a human model at 7 T. The transmit efficiency for the phantom was normalised to achieve the accepted power of 1 W and the transmit efficiency for the Duke model with/without the shield was normalised to attain the 10 g max. SAR of 1W. The calculated SAR values were scaled to accomplish the average transmit efficiency of 1 μT in the brain. The unit of the colour bars is $\mu T/\sqrt{W}$. The white straight and contour lines in the Duke model indicate the selected slice for the axial image and the selected brain region for the calculation of average B_1^+ and SARs, respectively. The table in the bottom row summaries the calculated values of B_1^+ and SARs.

a)	Tx insersion loss	Tx phase (degree)		
	dB	Measured value	Expected value	Difference
Ch1	-10.35	0	0	0
Ch2	-10.97	59.27	60	0.73
Ch3	-10.60	120.30	120	-0.30
Ch4	-10.43	181.89	180	-1.89
Ch5	-9.95	241.23	240	-1.23
Ch6	-9.80	299.79	300	0.21

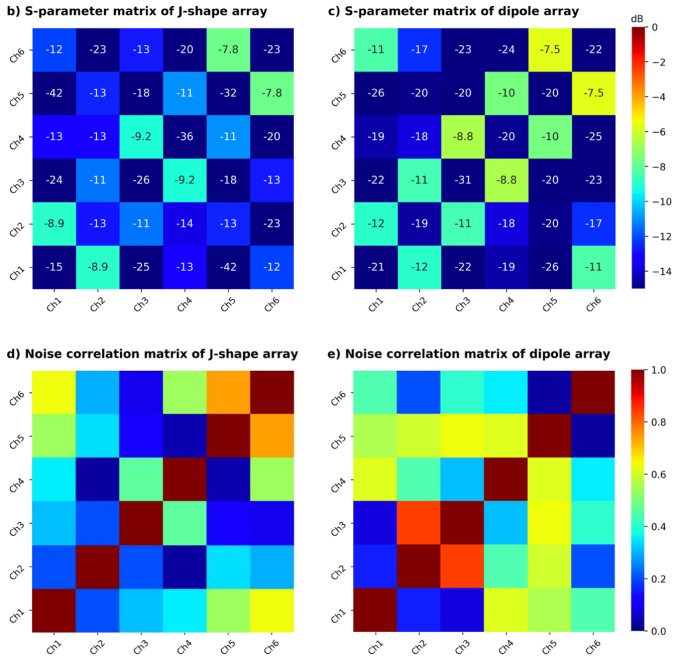

Fig. 6. Characteristics of the home-built RF interface (a) and S-parameter maps of the J-shape (b) and the dipole antenna array (c) measured on the bench using the network analyser. The noise correlation matrices are also shown (d, e).

IV. DISCUSSION

Although multi-modal imaging provides valuable information, it is always challenging to adapt the systems for simultaneous use and often results in performance degradation in at least one modality, therefore compromising the usefulness of these hybrid imaging systems. As one of the key requirements, in a simultaneous MR-PET or MR-SPECT experiment, the MRI RF probe must be placed inside the integrated systems. In this study, we have introduced and presented a new, gamma-radiation-transparent, RF antenna array concept for multi-modal combined systems. The MR performance of the new design has been demonstrated on a 7 T whole-body MRI scanner and the evaluation of potential gamma photon attenuation was carried out using a 511 keV transmission scan.

To aid accurate comparability with a conventional antenna array design, and due to the potential inter-element interference in the chosen diameter and length, we have initially presented a six-element J-shape antenna array design. In order to avoid any additional bias in performance caused by decoupling components, decoupling techniques were not applied. However, decoupling components can be employed on the J-shape antenna array (importantly, outside the PET FOV) and can undoubtedly further improve the decoupling factor. A number of decoupling methods suitable for use with radiating antenna arrays at ultra-high field MRI have been investigated and reported, e.g., using the magnetic wall [54, 55], induced current compensation or elimination (ICE) [56] and coupling matrix synthesis [57]. Employing such methods may allow us to further increase the total number of channels. This, together with the use of the parallel transmission (pTx) technique, possibly improves the sensitivity and the capability of sufficient B_1^+ control. Moreover, as there are more channels available for further adjustment and optimisation, SAR can be easily managed, and SAR hotspots are not expected. The pTx method is known to be useful for reducing SAR and improving B_1^+ homogeneity, particularly at ultra-high field MRI [58]. Instead of utilising a multiple Wilkinson's power divider assembly, RF transmission can, alternatively, be managed by using pTx which can be adapted in the current RF interface. By doing so, the transmit magnitudes and phases can be further flexibly adjusted and satisfactorily optimised to fit the object to be scanned. In this way and together with tailored RF pulses [59], signal voids or central brightening in the target region can be compensated and minimised.

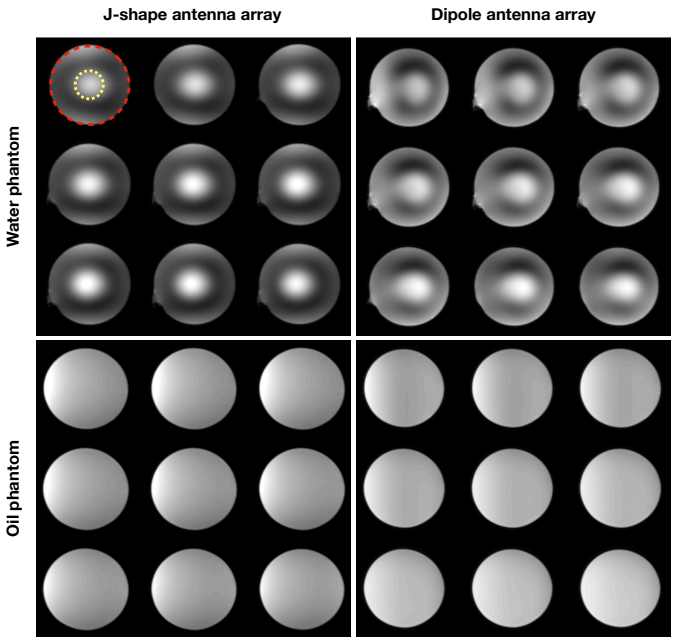

Fig. 7. Examples of multi-slice MR images acquired in the sagittal view using a sphere test object (water phantom: top row and oil phantom: bottom row): proposed J-shape antenna array (left column) and conventional dipole antenna array (right column). The ROIs (whole area: red dashed circle and centre region: yellow dotted circle) for the SNR calculation are also shown in the top left corner image.

In the J-shape antenna presented here, the radiating part and the feeding part were separated and soldered to link them together. However, both parts can be one solid single pattern built on e.g., PCB or wire without disconnection. This allows the J-shape antenna to be constructed with one material, typically using e.g., thin aluminium or copper stripe. For this

study, a copper strip was used for the radiating part and a copper wire was utilised for the feeding part. This was to aid ease of bending into the J shape as this design was absolutely novel in this application and flexible features were needed to investigate the characteristics of the J-shape antenna. The curved part (U-shape) may also be replaced by lumped elements, in order for its simplicity for setting up the J-shape antenna array although we need to conduct further detailed examinations and analysis and carry out additional comparisons with conventional designs before drawing any conclusions.

Furthermore, as the focus of this study was on the consequences of using the novel array design with both modalities, the effect of the 3D printed plastic former (material: polycarbonate, used as a base for both antenna arrays) on the detection quality using the transmission scans was not considered. However, the investigation of the 3D printed part used in this study has been carried out in our previous work, which shows that polycarbonate appears to be a suitable material for the use as an MR-PET coil former [21, 22, 60]. Nevertheless, this point could be further investigated and optimised by evaluating a range of different coil former materials and thicknesses in the future.

The simulation that we conducted used a continuous cylindrical with the material of perfect electrical conductor, since the main concern was to evaluate the effect of the inserted shield on B_1. More sophisticated shield designs, such as modular/segmented or overlapped, may be required in order to integrate this into the BrainPET insert consisting of eight staggered three-layer LSO detectors. It is also evident that further investigations on, e.g., the eddy current effect, on the scanner are needed.

To test stability of the tuning/matching condition by different subjects, we simply replaced the Duke model by the Ella model and used the identical simulation settings. We did not notice any dramatic detuning on any channels in the J-shape antenna array, and only a few dB of deviation (average of all channels: 0.6 dB) were apparent between two human voxel models in the S-parameter. This slight variation could mainly be due to the different loading condition.

There have been several previous efforts relating to the construction of hybrid MR-PET coils operating at the conventional field strengths with most design attempts moving all highly attenuating materials to outside the PET FOV, thus requiring a reduction of the number of channels, the extension of the coil length longer than the FOV, and the remote placement of the matching network and preamplifiers [61-63]. However, this type of design could degrade the performance / quality of the RF coil considerably when compared to its optimum condition without considering PET. In contrast to this, our proposed J-shape antenna array is intrinsically free from these problems. Another challenge using the conventional coils comes when they are used for ultra-high field MRI. Due to the requirement of unrealistic capacitor values for tuning, building an appropriate RF probe using traditional designs, e.g., birdcage coil or multi-loop array, is not readily achievable. The use of the travelling wave antenna approach [34], which does not have to be placed near the subject, is highly feasible but the receive sensitivity could be considerably decreased. Therefore, the dipole antenna and microstrip transmission line arrays are widely used and tend to be the key elements in use at ultra-high field MRI [33]. However, as shown above, placing high-density components inside the PET or SPECT detection region is unavoidable for these antenna arrays. Even though there are various disadvantages for certain applications, such as blocking the view for fMRI, a modified monopole antenna array [64] and an asymmetric dipole antenna array [57] may also be alternatives for hybrid imaging at ultra-high field.

The use of this new concept is not limited only to 7 T hybrid multi-modal imaging applications and can apparently be optimised for standalone MRI systems operating not only at 7 T but also at even higher field strengths, such as 9.4 T, 10.5 T and 11.7 T. In addition, the concept can also be implemented in certain applications at clinically relevant field strengths, e.g., 3 T body ^{1}H MR-PET imaging [65] and total-body PET systems [66]. Moreover, the proposed antenna design could be applied to investigate X-nuclei (non-proton nuclei that have comparatively lower gyromagnetic ratio and MR sensitivity and are closely connected to the biochemical and metabolic processes in the human body) if it is used as a body X-nucleus coil at ultra-high field [67]. In this context, the challenges would relate to optimising the physical structure of the X-nuclei J-shape antenna array for the useful FOV of the scanner and double-tuning the antenna to be also able to access ^{1}H functionality [68].

V. CONCLUSIONS

Here, we have introduced a novel J-shape antenna array concept, which is a unique MRI RF probe with exceptionally minimal gamma attenuation at 511 keV. The effect of using this new design was successfully evaluated according to the important features for both ultra-high field MRI and the transmission scan, and its practicability for the use with the ultra-high field MRI and its uniqueness with fusion MR-PET/SPECT systems were proved. Importantly, this gamma-radiation-transparent J-shape antenna array allows simultaneous MR-PET/SPECT experiments to be conducted without compromising any aspects of system performance and image quality compared to the standalone instrumentation.

ACKNOWLEDGEMENT

C-HC, LT, JS, ERK, CL and NJS are funded in part by the Helmholtz Validation Fund, “Next generation BrainPET scanner for 7 T MRI” Grant Nr. HVF-0051. The authors also thank Ms Rick for English proofreading.

REFERENCES

[1] K. Heinzmann, L.M. Carter, J.S. Lewis, E.O. Aboagye, “Multiplexed imaging for diagnosis and therapy,” *Nat. Biomed. Eng.,* vol 1, pp. 697–713, 2017.

[2] S.S. Gambhir, “Molecular imaging of cancer with positron emission tomography,” *Nat. Rev. Cancer,* vol 2, pp. 683–693, 2002.

[3] J.P. Greenwood, *et al.*, “Cardiovascular magnetic resonance and single-photon emission computed tomography for diagnosis of coronary heart disease (CE-MARC): a prospective trial,” *Lancet* vol. 379, pp. 453–460, 2012.

[4] T. Jones, E.A. Rabiner, "The development, past achievements, and future directions of brain PET," *J. Cereb. Blood. Flow Metab*., vol. 32, pp. 1426–1454, 2012.

[5] L.S. Kegeles, J.J. Mann, "In vivo imaging of neurotransmitter systems using radiolabeled receptor ligands," *Neuropsychopharmacology*, vol 17, pp. 293–307, 1997.

[6] W.-D. Heiss, "Hybrid PET/MR imaging in neurology: present applications and prospects for the future," *J. Nucl. Med*. vol. 57, pp. 993-995, 2016.

[7] J. Lamb, J.P. Holland, "Advanced Methods for Radiolabeling Multimodality Nanomedicines for SPECT/MRI and PET/MRI," *J. Nucl. Med*. vol. 59, pp. 382–389, 2018.

[8] M. Hamonet, *et al*., "The clearPET/XPAD prototype: development of a simultaneous PET/CT scanner for mice," *IEEE NSS/MIC*, pp. 1-3, 2015.

[9] N.J. Shah, *Hybrid MR-PET Imaging*. Cambridge, UK, RSC, 2018.

[10] A. Del Guerra, *et al*., "TRIMAGE: A dedicated trimodality (PET/MR/EEG) imaging tool for schizophrenia," *Eur. Psychiat*. vol. 50, pp. 7–20, 2018.

[11] M.S. Judenhofer, *et al*., "Simultaneous PET-MRI: a new approach for functional and morphological imaging," *Nat. Med*. vol. 14, pp. 459–465, 2008.

[12] B.F. Hutton, *et al*., "Development of clinical simultaneous SPECT/MRI," *Br. J. Radiol*. vol. 91, pp. 20160690, 2017.

[13] M. Occhipinti, *et al*., "Characterization of the Detection Module of the INSERT SPECT/MRI Clinical System," *IEEE Transactions on Radiation and Plasma Medical Sciences* vol. 2, pp. 554–563, 2018.

[14] C.E. Mader, T. Fuchs, D.A. Ferraro, I.A. Burger, "Potential Clinical Applications of PET/MR," *IEEE Transactions on Radiation and Plasma Medical Sciences* vol. 4, pp. 293–299, 2020.

[15] S. Song, *et al*., "Simultaneous FET-PET and contrast-enhanced MRI based on hybrid PET/MR improves delineation of tumor spatial biodistribution in gliomas: a biopsy validation study," *Eur. J. Nucl. Med. Mol. Imaging* vol. 47, pp. 1458–1467, 2020.

[16] A. Nowogrodzki, "The world's strongest MRI machines are pushing human imaging to new limits," *Nat*. vol. 563, pp. 24–26, 2018.

[17] M.E. Ladd, *et al*., "Pros and cons of ultra-high-field MRI/MRS for human application," *Prog. Nucl. Magn. Reson. Spectrosc*. vol. 109, pp. 1–50, 2018.

[18] L. Quettier, *et al*., "Commissioning Completion of the Iseult Whole Body 11.7 T MRI System," *IEEE Trans. Appl. Supercond*. vol. 30, pp. 1–5, 2020.

[19] G. Delso, A. Martinez-Möller, R.A. Bundschuh, R. Ladebeck, Y. Candidus, D. Faul, S.I. Ziegler, "Evaluation of the attenuation properties of MR equipment for its use in a whole-body PET/MR scanner," *Phys. Med. Biol*. vol. 55, pp. 4361-74, 2010.

[20] C. Weirich, D. Brenner, J. Scheins, E. Besancon, L. Tellmann, H. Herzog, N.J. Shah, "Analysis and correction of count rate reduction during simultaneous MR-PET measurements with the BrainPET scanner," *IEEE Trans. Med. Imaging* vol. 31, pp. 1372-1380, 2012.

[21] C.Y. Sander, *et al*., "A 31-channel MR brain array coil compatible with positron emission tomography," *Magn. Reson. Med*. vol. 73, pp. 2363–2375, 2015.

[22] M. Oehmigen, M.E. Lindemann, L. Tellmann, T. Lanz, H.H. Quick, "Improving the CT (140 kVp) to PET (511 keV) conversion in PET/MR hardware component attenuation correction," *Med. Phys*. vol. 47, pp. 2116-2127, 2020.

[23] L. Tellmann, H.H. Quick, A. Bockisch, H. Herzog, T. Beyer, "The effect of MR surface coils on PET quantification in whole-body PET/MR: results from a pseudo-PET/MR phantom study," *Med. Phys*. vol. 38, pp. 2795-2805, 2011.

[24] L. MacDonald, S. Kohlmyer, C. Liu, T.K. Lewellen, P.E. Kinahan, "Effects of MR surface coils on PET quantification," *Med. Phys*. vol. 38, pp. 2948-2956, 2011

[25] M. Eldib, *et al*., "Attenuation Correction for Magnetic Resonance Coils in Combined PET/MR Imaging: A Review," *PET Clinics* vol. 11, pp. 151–160, 2016.

[26] G. Delso, A. Martinez, R. Bundschuh, R. Ladebeck, D. Faul, S. Ziegler, "Study of MR head and neck coils for its use in an integrated MR/PET scanner," *J. Nucl. Med*. (suppl. 2), vol. 50, pp. 1476, 2009

[27] L. MacDonald, C. Liu, S. Kohlmyer, P. Kinahan, "Effects of MR coils on PET artifacts and quantification for multimodality PET/CT/MR scans," J. Nucl. Med. (suppl. 2), vol. 51, pp. 129, 2010.

[28] S.H. Keller, *et al*., "Image artifacts from MR-based attenuation correction in clinical, whole-body PET/MRI," MAGMA. vol. 26, pp. 173-181,2013.

[29] C.W. Lerche, *et al*., "PET attenuation correction for rigid MR Tx/Rx coils from 176Lu background activity," *Phys. Med. Biol*. vol. 63, pp. 035039, 2018.

[30] J.E. Mackewn, *et al*., "Practical issues and limitations of brain attenuation correction on a simultaneous PET-MR scanner," *EJNMMI Physics* vol. 7, pp. 24, 2020.

[31] A. Farag, *et al*., "Assessment of a novel 32-channel phased array for cardiovascular hybrid PET/MRI imaging: MRI performance," *Eur. J. Hybrid Imaging* vol. 3, pp. 13, 2019.

[32] M.S.H. Akram, T. Obata, T. Yaaya, "Microstrip transmission line RF coil for a PET/MRI insert," *Magn. Reson. Med. Sci*. vol. 19, pp.147-153, 2020

[33] A.J.E. Raaijmakers, *et al*., "The fractionated dipole antenna: A new antenna for body imaging at 7 Tesla," *Magn. Reson. Med*. vol. 75, pp. 1366–1374, 2016.

[34] D.O. Brunner, N. De Zanche, J. Fröhlich, J. Paska, K.P. Pruessmann, "Travelling-wave nuclear magnetic resonance," *Nat*. vol. 457, pp. 994–998, 2009.

[35] G. Duan, X. Zhao, S.W. Anderson, X. Zhang, "Boosting magnetic resonance imaging signal-to-noise ratio using magnetic metamaterials," *Commun. Phys*. vol. 2, pp. 1–8, 2019.

[36] M.J. Freire, L. Jelinek, R. Marques, M. Lapine, "On the applications of μr=-1 metamaterial lenses for magnetic resonance imaging," *J. Magn. Reson*. vol. 203, pp. 81–90, 2010.

[37] M.S.H. Akram, T. Obata, M. Suga, F. Nishikido, E. Yoshida, K. Saito, T. Yamaya, "MRI compatibility study of an integrated PET/RF-coil prototype system at 3T," *J. Magn. Reson*. vol. 283, pp. 62-70, 2017.

[38] P.D. Herrick, R.E. Ansorge, R.C. Hawkes, S.J. Sawiak, J.W. Stevick, T.A. Carpenter, "Radiofrequency coil design for simultaneous PET/MR systems," IEEE Nucl. Sci. Symp. Med. Imaging Conf. pp. 2560-2567, 2010.

[39] A.J.E. Raaijmakers, P.R. Luijten, C.A.T. van den Berg, "Dipole antennas for ultrahigh-field body imaging: a comparison with loop coils," *NMR Biomed*. vol. 29, pp. 1122–1130, 2016.

[40] J.J. Carr, G.W. Hippisley, *Practical antenna handbook*, 5th edition, New York, USA, McGraw-Hill Education, 2012

[41] B. Steensma, *et al*., "Introduction of the snake antenna array: Geometry optimization of a sinusoidal dipole antenna for 10.5T body imaging with lower peak SAR," *Magn. Reson. Med*. vol. 84, pp. 2885–2896, 2020.

[42] C. Stumpf, M. Malzacher, L.-P. Schmidt, "Radio Frequency Modeling of Receive Coil Arrays for Magnetic Resonance Imaging," *J. Imaging* vol. 4, pp. 67, 2018.

[43] M. Kozlov, R. Turner, "Fast MRI coil analysis based on 3-D electromagnetic and RF circuit co-simulation," *J. Magn. Reson*. vol. 200, pp. 147–152, 2009.

[44] C.W. Lerche, *et al*., "Design and estimated performance of a UHF-MRI compatible BrainPET insert for neuroscience," *IEEE NSS/MIC*, pp. 1130, 2020

[45] G. Shajan, C. Mirkes, K. Buckenmaier, J. Hoffmann, R. Pohmann, K. Scheffler, "Three-layered radio frequency coil arrangement for sodium MRI of the human brain at 9.4 tesla," *Magn. Reson. Med*. Vol. 75, pp. 906-916, 2016.

[46] S.-M. Hong, C.-H. Choi, N.J. Shah, J. Felder, "Design and evaluation of a 1H/31P double-tesonant helmet coil for 3T MRI of the brain," *Phys. Med. Biol*. vol. 64, pp. 035003, 2019.

[47] A. Destruel, J. Jin, E. Weber, M. Li, C. Engstrom, F. Liu, S. Crozier, "Integrated multi-modal antenna with coupled radiating structures (I-MARS) for 7T pTx body MRI," IEEE Trans. Med. Imaging, doi: 10.1109/TMI.2021.3103654.

[48] A. Christ, *et al*., "The Virtual Family—development of surface-based anatomical models of two adults and two children for dosimetric simulations," *Phys. Med. Biol*. vol. 55, pp. N23–N38, 2009.

[49] R. Brown, K. Lakshmanan, G. Madelin, P. Parasoglou, "A nested phosphorus and proton coil array for brain magnetic resonance imaging and spectroscopy," *NeuroImage* vol. 124, pp. 602-611, 2016.

[50] B. Wang, *et al*., "A radially interleaved sodium and proton coil array for brain MRI at 7 T," *NMR Biomed*. doi:10.1002/nbm.4608.

[51] I. Zivkovic, C.A. Castro, A. Webb, "Design and characterization of an eight-element passively fed meander-dipole array with improved specific absorption rate efficiency for 7 T body imaging," *NMR Biomed*. vol. 32, pp. e4106, 2019.

[52] A. Sadeghi-Tarakameh, *et al*., "Improving radiofrequency power and specific absorption rate management with bumped transmit elements in ultra-high field MRI," *Magn. Reson. Med*. vol. 84, pp. 3485-3493, 2020.

[53] G. Adriany, *et al*., "Transmit and Receive Transmission Line Arrays for 7 Tesla Parallel Imaging," *Magn. Reson. Med*. vol. 53, pp. 434–445, 2005.
[54] I.R.O. Connell, K.M. Gilbert, M.A. Abou-Khousa, R.S. Menon, "Design of a Parallel Transmit Head Coil at 7T With Magnetic Wall Distributed Filters," *IEEE Med. Imaging* vol. 34, pp. 836–845, 2015.
[55] I.R.O. Connell, K.M. Gilbert, M.A. Abou-Khousa, R.S. Menon, "MRI RF array decoupling method with magnetic wall distributed filters," *IEEE Med. Imaging* vol. 34, pp. 825–835, 2015.
[56] Y. Li, Z. Xie, Y. Pang, D. Vigneron, X. Zhang, "ICE decoupling technique for RF coil array designs," *Med. Phys*. vol. 38, pp. 4086-4093, 2011.
[57] I.R.O. Connell, R.S. Menon, "Shape Optimization of an Electric Dipole Array for 7 Tesla Neuroimaging," *IEEE Med. Imaging* vol. 38, pp. 2177–2187, 2019.
[58] F. Padormo, A. Beqiri, J.V. Hajnal, S.J. Malik, "Parallel transmission for ultrahigh-field imaging," *NMR Biomed*. vol. 29, pp. 1145–1161, 2016.
[59] V. Gras, A. Vignaud, A. Amadon, D.L. Bihan, N. Boulant, "Universal pulses: A new concept for calibration-free parallel transmission," *Magn. Reson. Med*. vol. 77, pp. 635–643, 2017.
[60] A. Celik, C.-H. Choi, L. Tellmann, C. Rick, N.J. Shah, J. Felder, "Design and construction of PET-compatible double-tuned 1H/31P MR head coil," Trans. Med. Imaging, DOI: 10.1109/TMI.2021.3070626.
[61] K. Lakshmanan, S. Dehkharghani, G. Madelin, R.A. Brown, "A dual-tuned 17O/1H head array for direct brain oximetry at 3 Tesla," *Magn. Reson. Med*. vol. 83, pp. 1512–1518, 2020.
[62] M. Oehmigen, *et al*., "A dual-tuned 13C/1H head coil for PET/MR hybrid neuroimaging: Development, attenuation correction, and first evaluation," *Med. Phys*. vol. 45, pp. 4877–4887, 2018.
[63] C.-H. Choi, *et al*., "Design, evaluation and comparison of endorectal coils for hybrid MR-PET imaging of the prostate," *Phys. Med. Biol*. vol. 65, pp. 115005, 2020.
[64] A.S.M.Z. Kausar, D.C. Reutens, E. Weber, V. Vegh, "Monopole antenna array design for 3 T and 7 T magnetic resonance imaging," *PLOS ONE* vol. 14, pp. e0214637, 2019.
[65] G. Delso, *et al*., "Performance Measurements of the Siemens mMR Integrated Whole-Body PET/MR Scanner," *J. Nucl. Med*. vol. 52, pp. 1914–1922, 2011.
[66] S.R. Cherry, *et al*., "Total-Body PET: Maximizing Sensitivity to Create New Opportunities for Clinical Research and Patient Care," *J. Nucl. Med*. vol. 59, pp. 3–12, 2018.
[67] L. Valkovič, *et al*., "Using a whole-body 31P birdcage transmit coil and 16-element receive array for human cardiac metabolic imaging at 7T," *PLOS ONE* vol. 12, pp. e0187153, 2017.
[68] C.-H. Choi, S.-M. Hong, J. Felder, N.J. Shah, "The state-of-the-art and emerging design approaches of double-tuned RF coils for X-nuclei, brain MR imaging and spectroscopy: A review," Magn. Reson. Imaging vol. 72, pp. 103-116, 2020.